J Sign Process Syst
DOI 10.1007/s11265-009-0435-3

Localizing Lung Sounds: Eigen Basis Decomposition for Localizing Sources Within a Circular Array of Sensors

S. M. A. Salehin · Thushara D. Abhayapala

Received: 28 May 2009 / Revised: 25 October 2009 / Accepted: 9 November 2009

Abstract Lung disorders or injury can result in changes in the production of lung sounds both spectrally and regionally. Localizing these lung sounds can provide information to the extent and location of the disorder. Difference in arrival times at a set of sensors and triangulation were previously proposed for *acoustic imaging* of the chest. We propose two algorithms for acoustic imaging using a set of eigen basis functions of the Helmholtz wave equation. These algorithms remove the sensor location contribution from the multi sensor recordings using either an orthogonality property or a least squares based estimation after which a spatial minimum variance (MV) spectrum is applied to estimate the source locations. The use of these eigen basis functions allows possible extension to a lung sound model consisting of layered cylindrical media. Theoretical analysis of the relationship of resolution to frequency and noise power was derived and simulations verified the results obtained. Further, a Nyquist's criteria for localizing sources within a circular array shows that the radius of region where sources can be localized is inversely proportional to the frequency of sound.The resolution analysis and modified Nyquist criteria can be used for determining the number of sensors required at a given noise level, for a required resolution, frequency range, and radius of region for which sources need to be localized.

S. M. A. Salehin (✉) · T. D. Abhayapala
Applied Signal Processing Group, Research School of Information Sciences and Engineering (RSISE), Australian National University, Canberra, Australian Capital Territory 0200, Australia
e-mail: asalehin@rsise.anu.edu.au

S. M. A. Salehin
National ICT Australia, Canberra, Australia

Keywords Localization · Lung sounds · Helmholtz equation · Basis decomposition · Cylindrical harmonics · Nyquist's criteria · Resolution

1 Introduction

Localization of lung sounds from multi-sensor recordings can be classified as a problem of source localization within a circular array of sensors. Ward et al. [1] showed how to locate a single source in the interior field of a sensor array. We propose algorithms to localize multiple sources within a circular array of sensors using cylindrical harmonic functions. It is advantageous to use these functions since propagation of layered cylindrical media can be analyzed by these functions and the chest can be modeled as consisting of cylindrical layered media. Performance metrics for the algorithms accounting for noise levels, frequency of sounds, and region of localization are derived. We apply a Minimum Variance (MV) spectrum to the processed sensor recordings to obtain high resolution localization algorithms.

The stethoscope since its invention in 1816 has been used as a first diagnosis tool for pulmonary, cardiac, and gastric disorders. The stethoscope allows physicians to diagnose the pulmonary system over the auditory range. This is useful since most physiological processes and structure of the body causes sounds that resonate in the audible sound range. The stethoscope is a non-invasive, quick and low cost diagnosis tool which can be used for out-patient home and field monitoring. The use of one stethoscope allows diagnosis from one location only and is qualitative being dependent on the skill of the physician. Multiple sensors to record data from several location simultaneously can be used to capture more information from the audible range of sounds produced by the lungs. Moreover, signal processing and statistical methods using microprocessors or computers can provide a quantitative analysis of lung sound data.

Research interest in localizing and analyzing lung sounds in the audible range was a result of the shortcomings of existing tools for lung diagnosis. These lung diagnosis methods involved using ultrasound techniques. However, ultrasound techniques have not been applied for lung diagnosis due to its poor performance with high frequency sounds (in the order of 1 MHz) [2]. This poor performance is caused by the high attenuation property of the lung parenchyma for high frequency sounds. Lung sound analysis with multiple stethoscopes can be used as a first diagnosis tool for lung disorders. Well established methods such as computed tomography (CT) and x-rays can later be applied to confirm the results obtained form the multiple stethoscope device. Diseases or injury can cause alterations in the structure and function of the lungs can cause changes in lung sound production and transmission. Lung consolidation, pneumothorax and airway obstructions are some of the conditions that can cause spectral and regional changes in lung sounds. If these changes are properly analyzed and localized from multi sensor recordings then the extent and location of the trauma can be acquired [3, 4].

Simultaneous recordings of breath sounds can be processed to provide a surface acoustic image of the thorax using interpolation [5]. Studies on healthy subjects and subjects with interstitial pneumothorax illustrated that thoracic surface *acoustic images*[1] can provide information on the spatial extent of the disease [6].

To get more information from the lung sounds researchers began to develop algorithms for localization of lung sounds in a 3D co-ordinate system. One of the earliest work on this was by Kompis et al. who presented a solution for acoustic imaging of the human chest [4]. His algorithm was independent of the time of arrival of lung sounds and used a triangulation approach to locate sound sources given that multiple sensor recordings were available. Kompis assumed a uniform sound speed throughout the whole thorax and a constant attenuation factor per unit length. This algorithm applied computer post-processing to recorded chest sounds obtained from multiple sensors placed on the chest. Kompis further went on to represent intrathoracic sound sources in a three dimensional distribution taking into account the thoracic volume. This algorithm was designed to be used for any number of sensors and be robust enough to deal with sensor failure or high noise levels. Kompis split the sensor recording using Tukey window functions [7] in the time domain and then transformed the resulting data into the frequency domain using the Fast Fourier Transform (FFT). This allowed the spatial sound source representation to be separated into multiple frequency bins. Kompis evaluated his algorithm using computer simulations, a gelatin model and human subjects. The resolution of Kompis's algorithm was reported from measurements to be 2 cm. Moreover, he was able to show that lung sound localization can give information on lung consolidation.

Other researchers tried to either incorporate a more accurate acoustic transmission model of the lung at the expense of the localizing algorithm or proposed better localizing algorithms simplifying the acoustic transmission model. Murphy assumed an isotropic velocity and calculated the locations of lung sounds based on differences in arrival times at the different sensors [8]. Other researchers used an experimentally determined focal index to localize lung sounds assuming free field propagation [9]. All the research mentioned previously developed algorithms on simplified model of lung sound propagation to the surface of the chest. Ozer et al. computationally and experimentally validated a boundary element for sound propagation within the chest [10]. The propagation model separated transmission through the parenchyma, and coupling to and transmission through tissue to reach the chest surface. Moreover, the model accounted for reflections, refractions and standing waves that may be present within the chest. Using this refined model of propagation, a matched field method was proposed for localizing sound sources. However, this algorithm cannot be applied for localizing multiple sources [10].

The aim of this paper is to propose and analyze sound localization algorithms within a circular sensor array applied to breath sounds. However, the algorithms can also be applied in sensor monitoring, hands free communication in a room or for recording sounds in an auditorium. The solution to the Helmholtz wave equation can be synthesized and analyzed for a cylindrical co-ordinate system with a set of eigen basis functions. These eigen basis functions are the cylindrical harmonics. The lung can be modeled as a layered cylindrical structure and propagation in such environments can include reflections and refractions and can

[1]Here acoustic imaging refers to obtaining the location of all sound sources, and is different from x-ray imaging and CT scans which show the lungs in a visual format.

be analyzed using cylindrical harmonic functions [11–13]. This paper aims to develop localizing algorithms using these eigen basis functions and investigates their performance under different conditions. The localizing algorithms rely on the eigen basis decomposition since this will allow easy extension to a layered cylindrical model of lung sound propagation. Further, these eigen basis function were shown to be versatile for direction-of-arrival (DOA) estimation [14].

The contributions made by the paper are discussed as follows:

- We propose two localizing algorithms using cylindrical harmonics with the aim of extending these algorithms for localizing sources within a layered cylindrical structure. The propagation through a layered cylindrical structure can be comparable to that of lung sounds propagating to the surface of the chest.
- The proposed algorithms will aim to use spectral search to locate source since spectral based methods are more accurate than triangulation. Further, methods using differences in arrival times require higher precision equipment than spectral based algorithms.
- We investigate the performance of the algorithms for different levels of noise and for different frequencies of sound.
- This paper also derives a relationship for resolution in terms of noise level and frequency for the proposed algorithms. This relationship will be useful in designing multi sensor systems for lung sound localization. Given the resolution required, noise levels and frequency range, the number of sensors can be determined for localizing sounds within a specific region.
- We prove that the Nyquist's criteria for localizing sources within a circular sensor array is different when compared to the Nyquist's theorem applied to linear arrays used for farfield beamforming.

This paper is organized as follows: Section 2 outlines the system model and defines the problem. Section 3 discusses a eigen basis decomposition method for wavefields. Section 4 presents two algorithms for lung sound localization that use this eigen decomposition. Section 5 provides theoretical analysis on the noise transformation, resolution and Nyquist's criteria for the proposed algorithms. Section 6 presents and describes the simulation results obtained for localizing sound sources using the proposed algorithms. Section 7 discusses some useful properties of the localizing algorithms and also presents a comparison of the two algorithms. Section 8 concludes this paper with a summary of major findings and discusses future work needed in acoustic imaging of the chest.

Notation

The notation used in this paper is a follows:

i	$= \sqrt{-1}$
$\boldsymbol{A}$	uppercase, bold letters represent matrices
$\boldsymbol{a}$	lowercase, bold letters represent vectors
$\boldsymbol{A}^T$	transpose of $\boldsymbol{A}$
$\boldsymbol{A}^*$	conjugate transpose of $\boldsymbol{A}$
$E\{.\}$	is the expectation operator
$\langle \boldsymbol{a}, \boldsymbol{b} \rangle$	inner product of vectors $\boldsymbol{a}$ and $\boldsymbol{b}$ defined as $\boldsymbol{a}^* \boldsymbol{b}$
$\lvert \cdot \rvert$	is the modulus operator

2 System Model

Lung sounds due to normal breathing are recorded by microphones placed on the chest as illustrated by Fig. 1. These microphone recordings can be processed to locate lung sounds. In this paper, we consider localizing two dimensional lung sound sources completely surrounded by a circular array of uniformly spaced sensors (microphones) placed at a radius, R. We assume that the velocity of the sound is isotropic. This was proved for lung sounds above 100 Hz using in vivo experiments [15].

The uniform spacing assumption is not a necessary condition, however it simplifies notation and

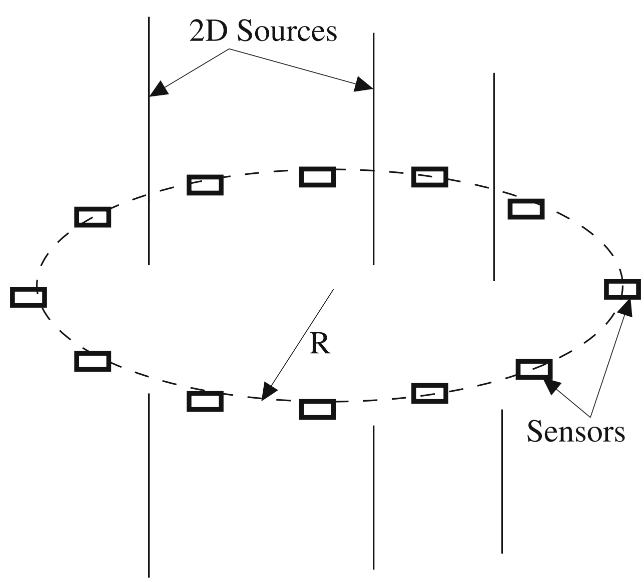

Figure 1 System model with lung sound sources located interior of a circular sensor array placed around the chest.

calculations. We assume that the source signals are zero mean and stationary. In most array signal processing literature, the sources are in the farfield such that the impinging wavefront is planar. The scenario presented in this paper is different and considers the sources to be in the nearfield with cylindrical impinging wavefronts.

Let there be Q sensors located at $\boldsymbol{x}_q$ with $q = 1, ..., Q$, where $\boldsymbol{x}_q \equiv (x_q,\ \theta_q)$, in polar coordinates, x_q is the distance from the origin and θ_q is the angle to the q^{th} sensor. For a circular array $x_q = R$ for all q. Assume that there are V sources present within the region enclosed by the sensors at locations $\boldsymbol{y}_v$ where $\boldsymbol{y}_v \equiv (y_v,\ \phi_v)$.

Lung sounds are broadband and the sensor data can be separated into different frequency bins by the Discrete Fourier Transform (DFT). The data captured by the sensors at a frequency bin with central frequency f_0 is

$$\boldsymbol{z}(k) = \sum_{v=1}^{V} \boldsymbol{a}(\boldsymbol{y}_v, k) s_v(k) + \boldsymbol{n}(k) \tag{1}$$

where

- k — is the wavenumber and $k = 2\pi f_0/c$ with c as the speed of propagation,
- $\boldsymbol{z}(k)$ — is the $Q \times 1$ vector of sensor recordings,
- $\boldsymbol{n}(k)$ — is the $Q \times 1$ vector containing additive noise,
- $s_v(k)$ — is the signal emitted by the v^{th} source as received at the origin, and
- $\boldsymbol{a}\left(\boldsymbol{y}_v, k\right)$ — is the *array manifold vector* generated by a source located at $\boldsymbol{y}_v$.

The array manifold vector is composed of elements that contain information on the attenuation and the phase change as the wave propagates from the source location to the sensors and is defined by

$$\boldsymbol{a}\left(\boldsymbol{y}_v, k\right) \triangleq \left[B\left(\boldsymbol{x}_1, \boldsymbol{y}_v, k\right),\ \ldots,\ B\left(\boldsymbol{x}_Q, \boldsymbol{y}_v, k\right)\right]^T \tag{2}$$

where

$$B\left(\boldsymbol{x}, \boldsymbol{y}, k\right) = \frac{i}{4} H_0^{(1)}\left(k|\boldsymbol{x} - \boldsymbol{y}|\right). \tag{3}$$

$B(\boldsymbol{x}, \boldsymbol{y}, k)$ is the Green's function which is the fundamental solution to the 2D Helmholtz equation. The term $H_0^{(1)}(\cdot)$ is the Hankel function of the first kind and zeroth order. The Hankel function of the first kind is used since the wavefield is radiating away from the origin. An example of a 2D wavefield for $k = 2$ (frequency of 108 Hz in air with speed of sound 340 m/s) is illustrated in Fig. 2. For multiple sources, the principle of superposition can be applied to derive the wavefield magnitude and phase at vector point $\boldsymbol{x}$.

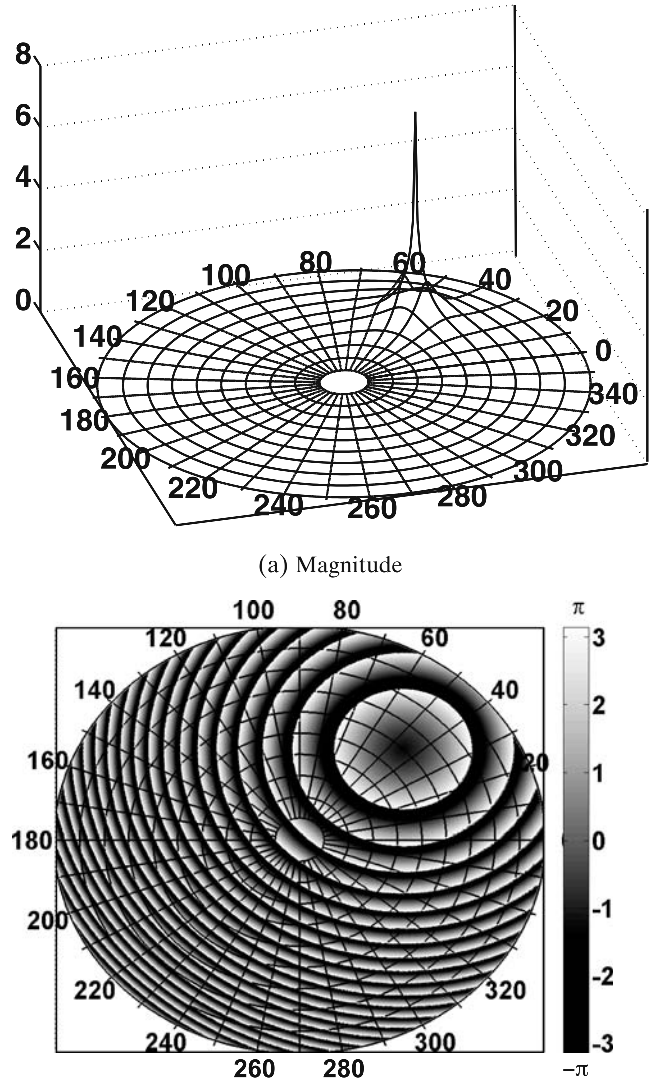

Figure 2 Wavefield generated by a 2-D source at $[3, \pi/4]$. The field magnitude at the source location is infinity and the magnitude dies down very sharply. The phase information can be expected to be more different at the sensors than the magnitude.

Note that for a farfield case using linear arrays, the array manifold entries for different sensors changes in phase only.[2] However, for our case involving cylindrical wavefronts, the entries in the array manifold change in both magnitude and phase for different sensor recordings as illustrated in Fig. 2.

Previous work [1] for locating sources contained in the interior of a sensor array is only applicable for localizing a single source and uses an optimization trans-

[2] $\boldsymbol{a}(\theta_v, k) \triangleq \left[e^{ik\boldsymbol{x}_1 sin(\phi)},\ \ldots,\ e^{ik\boldsymbol{x}_Q sin(\phi)}\right]^T$ where ϕ is the DOA.

formation to cancel out the magnitude changes. This optimization transformation cannot be applied when multiple sources are involved. The algorithm developed in this paper takes into account both the magnitude and the phase variation between sensors in order to locate multiple sources.

Localization algorithms discussed in this paper will consider narrowband sources. This can be easily extended to a broadband scenario since broadband signals can be decomposed to a set of narrowband bins by applying a set of narrowband filters to the sensor data. The DFT decomposes the array data to different frequency bins and the proposed localization algorithms are applied independently to each of these bins. For the rest of this paper, we will be considering data from only one frequency bin, therefore rewriting Eq. 1 in matrix notation and ignoring k for the narrowband case, we have

$$\boldsymbol{z} = \boldsymbol{A}(\boldsymbol{Y})\boldsymbol{s} + \boldsymbol{n} \tag{4}$$

where

$$\boldsymbol{A}(\boldsymbol{Y}) = \left[\boldsymbol{a}(y_1), \ldots, \boldsymbol{a}(y_v)\right], \tag{5}$$

$$\boldsymbol{Y} = \left[\boldsymbol{y}_1, \ldots, \boldsymbol{y}_v\right] \tag{6}$$

and

$$\boldsymbol{s} = \left[\boldsymbol{s}_1, \ldots, \boldsymbol{s}_v\right]^T. \tag{7}$$

Direction of Arrival (DOA) methods aim to determine the angle only, however the localization problem, considered in this paper, is set up similar to a DOA problem but aims to estimate $\boldsymbol{Y}$ which includes both the range and angle in polar co-ordinates. In a similar fashion to DOA methods, the localization algorithms will use the correlation matrix of the received data which is

$$\boldsymbol{R}_z = E\{\boldsymbol{z}\boldsymbol{z}^*\}. \tag{8}$$

By substituting Eq. 4 into Eq. 8 and assuming that the noise and source signals are uncorrelated, the correlation matrix is equivalent to

$$\boldsymbol{R}_z = \boldsymbol{A}(\boldsymbol{Y})E\{\boldsymbol{s}\boldsymbol{s}^*\}\boldsymbol{A}(\boldsymbol{Y})^* + E\{\boldsymbol{n}\boldsymbol{n}^*\}. \tag{9}$$

3 Eigen Basis Decomposition

A sensor array captures information on the impinging wavefield which can be decomposed to a set of orthogonal basis functions depending on the spatial coordinates used. These basis sets are useful for synthesizing and analyzing wavefield information captured by a sensor array. For a three dimensional wavefield, spherical harmonics form the basis sets and for a two dimensional wavefield, as investigated in this paper, cylindrical harmonics make up the basis set.

Eigen basis functions for wavefields have been applied in research pertaining to antennas. Works [16, 17] used eigen basis modes to synthesize antenna shapes. In beamforming, eigen basis modes were used for designing nearfield broadband beamformers [18, 19]. Moreover, in acoustic signal processing, these basis modes were applied to soundfield recording [20] and reproduction [21]. More importantly, sound propagation through the chest can be modeled similar to a layered cylindrical media. Eigen basis modes or more specifically cylindrical harmonics have been applied to wave propagation in layered cylindrical media [11–13].

The two dimensional wavefield investigated in this paper can be decomposed to basis functions [22, p. 66]

$$B(\boldsymbol{x}, \boldsymbol{y}) = \frac{i}{4}\sum_{n=-\infty}^{\infty} H_n^{(1)}(kx)J_n(ky)e^{in\theta_x}e^{-in\phi_y} \tag{10}$$

where $J_n(\cdot)$ is the Bessel function of order n. This decomposition consists of an infinite number of terms and is called the addition theorem for Hankel functions, valid only when $|\boldsymbol{x}| > |\boldsymbol{y}|$. The decomposition can be used if the significant number of terms are finite. The Bessel functions of finite argument approach zero as the order n becomes large. Therefore, for a finite region of space bounded by a circle of radius, R and for the wave length of sound being λ, the number of eigen basis functions that characterize a wavefield without incurring significant errors [23] can be limited to

$$M = \left\lceil \frac{\pi e R}{\lambda} \right\rceil \approx kR. \tag{11}$$

In the truncated 2D wavefield decomposition, the order, n spans the set $n \in [-M, \ldots, 0, \ldots, M]$ in Eq. 10. In the rest of this paper, the truncated 2D Green's function approximated by $2M+1$ basis functions is denoted by $\widetilde{B}(\boldsymbol{x}, \boldsymbol{y})$.

4 Sound Localization

The cylindrical waves impinging on the sensor array caused by 2D sources, results in an array manifold defined by

$$\boldsymbol{A}(\boldsymbol{Y}) = \begin{bmatrix} \widetilde{B}(\boldsymbol{x}_1, \boldsymbol{y}_1) & \ldots & \widetilde{B}(\boldsymbol{x}_1, \boldsymbol{y}_V) \\ \vdots & \ddots & \vdots \\ \widetilde{B}(\boldsymbol{x}_Q, \boldsymbol{y}_1) & \ldots & \widetilde{B}(\boldsymbol{x}_Q, \boldsymbol{y}_V) \end{bmatrix}. \tag{12}$$

The elements in $\boldsymbol{A}(\boldsymbol{Y})$ represent both the magnitude and phase difference of wavefields received by the sensors. Further, these elements can be represented by Eq. 3 or by the summation of eigen basis modes Eq. 10. Source and sensor location information are present in the elements of $\boldsymbol{A}(\boldsymbol{Y})$. However, by considering these elements as the sum of eigen basis modes, we can separate $\boldsymbol{A}(\boldsymbol{Y})$ into two independent terms containing sensor locations and source locations, respectively. The two proposed algorithms presented in the next two subsections exploit the idea that the sensor location terms can be removed from the array manifold, $\boldsymbol{A}(\boldsymbol{Y})$ and then source locations can be estimated using spectral techniques.

4.1 Orthogonality Based Algorithm

4.1.1 Fourier Series Expansion

The angular positions of the sensors span the range $[0, 2\pi]$, allowing exploitation of the orthogonality property of exponential functions, $e^{in\theta}$. Let $z(\theta)$ be a continuous function denoting the received signal for a sensor placed at an angle θ. This continuous function $z(\theta)$ is periodic on 2π and can be expressed as

$$z(\theta) = \sum_{n=-M}^{M} \alpha_n^{(R)} e^{in\theta} \tag{13}$$

where $\alpha_n^{(R)}$ is called the spatial Fourier coefficients of the sensor data for mode n. We can view Eq. 13 as a Fourier series expansion of the received signal. By multiplying both sides of Eq. 13 by $e^{-in\theta}$ and integrating with respect to θ over $[0, 2\pi)$, we obtain

$$\alpha_n^{(R)} = \frac{1}{2\pi} \int_0^{2\pi} z(\theta) e^{-in\theta}\, \mathrm{d}\theta. \tag{14}$$

From Eq. 1

$$z(\theta) = \sum_{v=1}^{V} B\left((R,\theta),\, \boldsymbol{y}_v\right) s_v + n(\theta) \tag{15}$$

where $n(\theta)$ is the AWGN (additive white, Gaussian noise) at a sensor placed at an angle θ on the circular array. Substituting Eqs. 10 and 15 into Eq. 14, we get

$$\alpha_n^{(R)} = \frac{i}{8\pi} H_n^{(1)}(kR) \sum_{v=1}^{V} J_n(ky_v) e^{-in\phi_v} + \widetilde{n}_n. \tag{16}$$

where $\widetilde{n}_n$ is the noise for the spatial Fourier coefficient at mode n. Writing Eq. 16 in matrix notation

$$\boldsymbol{\alpha} = \boldsymbol{H}\boldsymbol{J}\boldsymbol{s} + \widehat{\mathbf{n}} \tag{17}$$

where $\boldsymbol{\alpha} = 8\pi/i\left[\alpha_{-M}^{(R)}, \ldots, \alpha_M^{(R)}\right]^T$, $\boldsymbol{H} = diag\left[H_{-M}^{(1)}(kR), \ldots, H_M^{(1)}(kR)\right]$ and $\boldsymbol{J}$ contains information on the source locations

$$\boldsymbol{J} = \begin{bmatrix} J_{-M}(ky_1)e^{iM\phi_1} & \ldots & J_{-M}(ky_V)e^{iM\phi_V} \\ \vdots & \ddots & \vdots \\ J_M(ky_1)e^{-iM\phi_1} & \ldots & J_M(ky_V)e^{-iM\phi_V} \end{bmatrix}. \tag{18}$$

The spatial Fourier coefficients comprise of terms dependent on the positions of the V sources and the radius at which the sensors are placed. Contributions of the sensor angular positions are removed by transforming the array data to a spatial Fourier domain Eq. 14.

4.1.2 Discrete Angular Samples

In practice, we measure $z(\theta)$ only on discrete sensor positions at θ_q, $q = 1 \ldots Q$. Thus, one can approximate the integral Eq. 14 by a summation

$$\alpha_n^{(R)} = \frac{1}{2\pi} \sum_{q=q}^{Q} z\left(\theta_q\right) e^{-in\theta} \Delta\theta_q \tag{19}$$

where $\Delta\theta_q$ is the angular separation between the q^{th} and $(q+1)^{th}$ sensors. If the sensors are uniformly spaced on the circle, then Eq. 19 can be viewed as a Discrete Fourier Transform. The operations required to transform the discrete sensor data to the spatial Fourier domain are summarized[3] in Fig. 3. We write Eq. 19 in matrix form as

$$\boldsymbol{\alpha} = \frac{4}{iQ} \boldsymbol{\Xi}^* \boldsymbol{z} \tag{20}$$

where

$$\boldsymbol{\Xi} = \begin{bmatrix} e^{-iM\theta_1} & \ldots & e^{iM\theta_1} \\ \vdots & \ddots & \vdots \\ e^{-iM\theta_Q} & \ldots & e^{iM\theta_Q} \end{bmatrix}. \tag{21}$$

and the columns of $\boldsymbol{\Xi}$ are the Q discrete samples of the orthonormal function $e^{in\theta}$.

The spatial Fourier coefficients has a component that is dependent on the radial positions of the sensor. This algorithm aims to transform the sensor data to a domain dependent only on the source locations. This

[3] The discrete form of the orthogonality relationship for exponential functions applied in Eq. 19 is valid only if there is no aliasing. A discrete number of sensors sample the imping wavefront and is analogous to sampling the function $e^{in\theta}$ at the angular positions of the sensors. For large n, a greater number of sensors spanning the circumference of a circle is required in order to avoid aliasing.

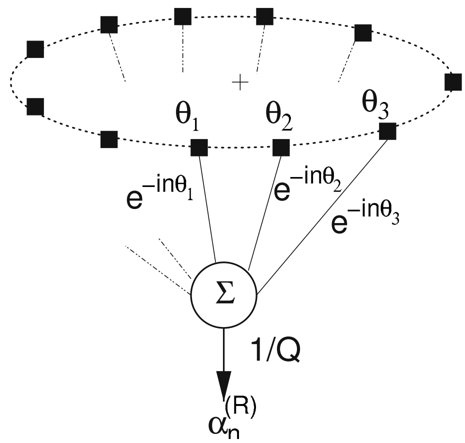

Figure 3 Transformation of the sensor data to the spatial Fourier domain.

would create a unified representation for data recorded by different sensor arrays for an impinging wavefield caused by sources in the same locations. However, removal of the matrix $\boldsymbol{H}$ from the spatial Fourier coefficients by using its inverse can cause instability of the solution when the condition number, $\kappa\{\boldsymbol{H}\}$ is large.

If the radial sensor components are not removed then the source locations can be estimated by first calculating the covariance matrix of the spatial Fourier coefficients, $\boldsymbol{R}_\alpha$ by

$$\boldsymbol{R}_\alpha = E\{\boldsymbol{\alpha}\boldsymbol{\alpha}^*\}. \tag{22}$$

In practice, the covariance matrix is not acquirable. However, $\boldsymbol{\alpha}$ can be obtained for a finite number of snapshots, T. Then a maximum likelihood approximation

$$\boldsymbol{R}_\alpha \approx \frac{1}{T}\sum_{t=1}^{T}\boldsymbol{\alpha}(t)\boldsymbol{\alpha}(t)^* \tag{23}$$

can be used to estimate $\boldsymbol{R}_\alpha$. It is important to mention that maximum likelihood approximations improve if the value of T is larger.

The Minimum Variance (MV) or the Capon's method [24] was developed to overcome poor resolution methods that were available in classical beamforming. The MV method passes the signal from the look direction and minimizes the output power from all other directions. The output power of the circular sensor array as a function of y and ϕ is given by the MV spatial spectrum

$$\widetilde{Z}(y,\phi) = \frac{1}{\boldsymbol{d}(R,y,\phi)^*\boldsymbol{R}_\alpha^{-1}\boldsymbol{d}(R,y,\phi)} \tag{24}$$

where

$$\boldsymbol{d}(R,y,\phi) = \begin{bmatrix} H_{-M}^{(1)}(kR)J_{-M}(ky)e^{iM\Phi} \\ \vdots \\ H_M^{(1)}(kR)J_M(ky)e^{-iM\phi} \end{bmatrix}. \tag{25}$$

The spectrum is computed and plotted over the whole range of y and ϕ. It is important to mention that the spacing of the y and ϕ in computing the spectrum must be smaller than the resolution of the MV method. Form the MV spatial spectrum, the source locations are estimated by locating the peaks in the spectrum.

If the condition number, $\kappa\{\boldsymbol{H}\}$ is small, we can remove the sensor radial component by

$$\widetilde{\boldsymbol{\alpha}} = \boldsymbol{H}^{-1}\boldsymbol{\alpha} \tag{26}$$

where

$$\boldsymbol{H}^{-1} = diag\left[\frac{1}{H_{-M}^{(1)}(kR)}, \;\cdots,\; \frac{1}{H_0^{(1)}(kR)}, \;\cdots,\; \frac{1}{H_M^{(1)}(kR)}\right]. \tag{27}$$

and $\widetilde{\boldsymbol{\alpha}}$ is called the modal space or the eigen space domain of the sensor array data. The covariance matrix of $\widetilde{\boldsymbol{\alpha}}$ can be estimated by the maximum likelihood approximation

$$\boldsymbol{R}_{\widetilde{\alpha}} \approx \frac{1}{T}\sum_{t=1}^{T}\widetilde{\boldsymbol{\alpha}}(t)\widetilde{\boldsymbol{\alpha}}(t)^* \tag{28}$$

and the source locations are the peaks in the new MV spectrum

$$Z(y,\phi) = \frac{1}{\boldsymbol{c}(y,\phi)^*\boldsymbol{R}_{\widetilde{\alpha}}^{-1}\boldsymbol{c}(y,\phi)} \tag{29}$$

where

$$\boldsymbol{c}(y,\phi) = \begin{bmatrix} J_{-M}(ky)e^{iM\phi} \\ \vdots \\ J_M(ky)e^{-iM\phi} \end{bmatrix}. \tag{30}$$

Comparing Eqs. 24 and 29, the MV spectrum when the radial component is removed is less computationally expensive since computing $\boldsymbol{d}(R,y,\phi)$ for the entire range of y and ϕ is more expensive than computing $\boldsymbol{c}(y,\phi)$.

In normal DOA scenarios, the MV spectrum is less computationally expensive since the spectrum is obtained as a function of one variable, the DOA. Further, the MV spectrum can be computationally expensive for a large sensor array as it requires the computation of a matrix inverse. Note that high resolution subspace methods such as MUSIC [25] can be applied to the orthogonality based algorithm in place of the MV spatial spectrum.

4.1.3 Condition Number of $\boldsymbol{H}$

The Hankel function is a complex function with a corkscrew like behavior with increasing argument. Since $H_{-n}^{(1)}(kR) = e^{i\pi n} H_n^{(1)}(kR)$, we have $\left|H_{-n}^{(1)}(kR)\right| = \left|H_n^{(1)}(kR)\right|$ and so the condition number for matrix $\boldsymbol{H}$, $\kappa\{\boldsymbol{H}\} = \left|H_M^{(1)}(kR)\right| / \left|H_0^{(1)}(kR)\right|$. If $\kappa\{\boldsymbol{H}\}$ is large, then removing $\boldsymbol{H}$ by multiplying $\boldsymbol{\alpha}$ by $\boldsymbol{H}^{-1}$ can result in instability of the solution since noise is amplified and the results obtained for the source locations will be practically useless. However, in such cases regularization methods can be applied resulting in a degradation of resolution in the solutions obtained.

Further, the magnitude of the Hankel functions increase with the mode n for a given argument, so the greater the number of modes used the larger the value of $\kappa\{\boldsymbol{H}\}$, but $\kappa\{\boldsymbol{H}\}$ decreases as values of kR get larger (for cases when kR is a real number with zero imaginary component). From Fig. 4, we can see that as a rule of thumb if $kR > 0.75 \times M$ then $\kappa\{\boldsymbol{H}\}$ is small (in this definition we ensure that $\kappa\{\boldsymbol{H}\} < 10^2$) thus ensuring a stable solution when $\boldsymbol{H}^{-1}$ is multiplied to α.

If the sensor radial component is to be removed, there are two conditions that need to be considered when choosing the number of modes to use, given both the wavenumber, k and the radius of the region of interest, R. These two conditions include the stability condition and Eq. 11 resulting in M being

$$kR < M < \frac{4}{3}kR. \tag{31}$$

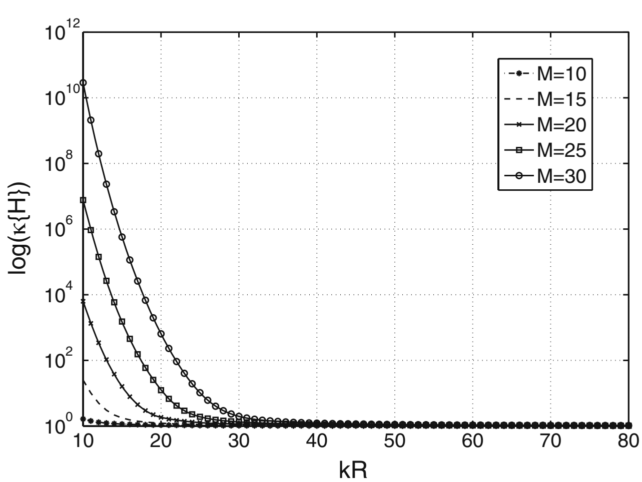

Figure 4 Variation of the condition number $\kappa\{\boldsymbol{H}\}$ with kR and number of modes (M) used.

4.2 Least Squares Based Algorithm

Similar to the orthogonality based algorithm, the least squares based algorithm removes the sensor contributions to transform the sensor array data to a eigen basis domain, $\widetilde{\boldsymbol{\alpha}}$. The source locations can be estimated by peaks in the MV spectrum Eq. 29 after an estimate of the covariance matrix in the eigen space domain is calculated Eq. 28.

From Eq. 10, each element in the array manifold matrix, $\boldsymbol{A}(\boldsymbol{Y})$ consists of summation of orthogonal basis functions of 2D wavefields. Therefore, the matrix $\boldsymbol{A}(\boldsymbol{Y})$ can be separated into two matrices as

$$\boldsymbol{A}(\boldsymbol{Y}) = \frac{i}{4}\boldsymbol{\Gamma}\boldsymbol{\Upsilon} \tag{32}$$

where

$$\boldsymbol{\Gamma} = \begin{bmatrix} H_{-M}^{(1)}(kR)e^{-iM\theta_1} & \dots & H_M^{(1)}(kR)e^{iM\theta_1} \\ \vdots & \ddots & \vdots \\ H_{-M}^{(1)}(kR)e^{-iM\theta_Q} & \dots & H_M^{(1)}(kR)e^{iM\theta_Q} \end{bmatrix} \tag{33}$$

and

$$\boldsymbol{\Upsilon} = \begin{bmatrix} J_{-M}(ky_1)e^{iM\phi_1} & \dots & J_{-M}(ky_V)e^{iM\phi_V} \\ \vdots & \ddots & \vdots \\ J_M(ky_1)e^{-iM\phi_1} & \dots & J_M(ky_V)e^{-iM\phi_V} \end{bmatrix}. \tag{34}$$

One of these matrices, $\boldsymbol{\Gamma}$ contains data on the sensor locations. The other matrix, $\boldsymbol{\Upsilon}$ contains the data on the source locations.

From the array manifold, we need to remove the contribution of sensor locations. Given that the sensor locations are known, we can construct the matrix, $\boldsymbol{\Gamma}$. The contribution of the sensor locations from the sensor recording vector, $\boldsymbol{z}$ can be removed by using the Moore-Penrose pseudo-inverse of $\boldsymbol{\Gamma}$, denoted by $\boldsymbol{\Gamma}^{\dagger}$.This pseudo-inverse is

$$\boldsymbol{\Gamma}^{\dagger} = [\boldsymbol{\Gamma}^{*}\boldsymbol{\Gamma}]^{-1}\boldsymbol{\Gamma}^{*}. \tag{35}$$

Multiplying the sensor recording vector by the pseudo inverse, $\widetilde{\boldsymbol{\alpha}} = 4/i\boldsymbol{\Gamma}^{\dagger}\boldsymbol{z} = \boldsymbol{\Upsilon}\boldsymbol{s} + \widehat{\boldsymbol{n}}$, transforms the data to the modal space, with $\widetilde{\boldsymbol{\alpha}}$ containing the source location matrix and the modified noise is denoted by $\widehat{\boldsymbol{n}}$. This operation is equivalent to a least squares approximation.

4.2.1 Pseudo-Inverse of $\boldsymbol{\Gamma}$

The calculation of the Moore-Penrose pseudo-inverse for $\boldsymbol{\Gamma}$ is equivalent to Eq. 35 only when $\boldsymbol{\Gamma}$ is not close to being singular. From trials constructing $\boldsymbol{\Gamma}$ for several different arrangement in a circular array, it was observed that in most cases $\boldsymbol{\Gamma}$ was close to singular. The reason for $\boldsymbol{\Gamma}$ being close to singular in certain situations is because elements in $\boldsymbol{\Gamma}$ can only be approximated to a certain number of decimal places and the magnitude of these elements can be very small. In such a case, $\boldsymbol{\Gamma}^{\dagger}$ can be calculated by using Singular Value Decomposition (SVD). The SVD of $\boldsymbol{\Gamma} \in \mathbb{C}^{Q\times(2M+1)}$ is

$$\boldsymbol{\Gamma} = \boldsymbol{U}\boldsymbol{D}\boldsymbol{F}^{*} \tag{36}$$

where $\boldsymbol{U} \in \mathbb{C}^{Q\times Q}$ and $\boldsymbol{F} \in \mathbb{C}^{(2M+1)\times(2M+1)}$ are orthogonal matrices, and $\boldsymbol{D}$ is a $Q \times (2M+1)$ diagonal matrix

$$\boldsymbol{D} = \begin{bmatrix} \xi_1 & 0 & 0 & \dots & 0 & 0 & \dots & 0 \\ 0 & \xi_2 & 0 & \dots & 0 & 0 & \dots & 0 \\ 0 & 0 & \xi_3 & \dots & 0 & 0 & \dots & 0 \\ \vdots & \vdots & \vdots & \dots & \vdots & \vdots & \dots & \vdots \\ 0 & 0 & 0 & \dots & \xi_p & 0 & \dots & 0 \end{bmatrix} \tag{37}$$

where ξ_i are the singular values of $\boldsymbol{\Gamma}$ with $p = min\left[Q,\ 2M+1\right]$ and $\xi_1 > \xi_2 > \dots > \xi_p > 0$.

From Eq. 37, $\boldsymbol{\Gamma}^{\dagger}$ can be obtained by

$$\boldsymbol{\Gamma}^{\dagger} = \boldsymbol{F}\boldsymbol{D}^{\dagger}\boldsymbol{U}^{*} \tag{38}$$

where

$$\boldsymbol{D}^{\dagger} = \begin{bmatrix} \frac{1}{\xi_1} & 0 & 0 & \dots & 0 \\ 0 & \frac{1}{\xi_2} & 0 & \dots & 0 \\ 0 & 0 & \frac{1}{\xi_3} & \dots & 0 \\ \vdots & \vdots & \vdots & \dots & \vdots \\ 0 & 0 & 0 & \dots & \frac{1}{\xi_p} \\ 0 & 0 & 0 & \dots & 0 \\ \vdots & \vdots & \vdots & \dots & \vdots \\ 0 & 0 & 0 & \dots & 0 \end{bmatrix}. \tag{39}$$

For more information on the Moore-Penrose pseudo-inverse, the reader is referred to the article [26].

5 Theoretical Performance Analysis

5.1 Noise

In this section, we analyze how the measurement noise at each sensor affects the performance of the proposed localization algorithms. We assume that the additive noise at each sensor is zero mean white, complex Gaussian and the noise at different sensors are uncorrelated. The covariance of the noise matrix is

$$\boldsymbol{R}_n = E\{\boldsymbol{n}\boldsymbol{n}^{*}\} = \sigma_n^2\boldsymbol{I} \tag{40}$$

where σ_n^2 is the noise power at each sensor and $\boldsymbol{I}$ represents an identity matrix. In literature, DOA algorithms applied to scenarios with correlated noise such as sonar applications led to biasing of the estimate and a degradation in resolution [27]. In this subsection, we analyze what effect the two proposed algorithms have on the noise covariance matrix and if these transformations result in the noise being correlated.

Firstly, for the orthogonality based algorithm, the noise covariance matrix after transformation into the eigen basis domain becomes

$$\tilde{\boldsymbol{R}}_n = E\left\{\hat{\boldsymbol{n}}\hat{\boldsymbol{n}}^{*}\right\} = \left(\frac{4}{Q}\right)^2 \sigma_n^2\boldsymbol{H}^{-1}\boldsymbol{\Xi}^{*}\boldsymbol{\Xi}\left(\boldsymbol{H}^{-1}\right)^{*}. \tag{41}$$

Since the series $\{e^{in\theta}\}_{n=-M}^{M}$ is orthogonal, $\boldsymbol{\Xi}^{*}\boldsymbol{\Xi} = Q\boldsymbol{I}$. Further,

$$\begin{aligned} &\boldsymbol{H}^{-1}\left(\boldsymbol{H}^{-1}\right)^{*} \\ &= (\boldsymbol{H}\boldsymbol{H}^{*})^{-1} = (\boldsymbol{H}^{*}\boldsymbol{H})^{-1} \\ &= diag\left[\frac{1}{\left|H_{-M}^{(1)}(kR)\right|^2},\ \dots,\ \frac{1}{\left|H_{0}^{(1)}(kR)\right|^2},\ \dots,\ \frac{1}{\left|H_{M}^{(1)}(kR)\right|^2}\right]. \end{aligned} \tag{42}$$

and the modified covariance matrix can be simplified to

$$\tilde{\boldsymbol{R}}_n = \frac{16}{Q}\sigma_n^2(\boldsymbol{H}^{*}\boldsymbol{H})^{-1}. \tag{43}$$

From Eq. 43, the structure of the noise covariance matrix remains diagonal meaning that the noise at the different modes are uncorrelated after the transformation to the new basis domain. The transformation of sensor recordings in the eigen basis domain creates an analogy between the noise at the sensors and the noise at the different modes. Further, the noise distribution remains Gaussian but is scaled differently at the different modes.

Secondly, for the least squares based algorithm, the noise covariance matrix after transforming the received data into the eigen basis domain becomes

$$\begin{aligned} \tilde{\boldsymbol{R}}_n &= 16\sigma_n^2\boldsymbol{\Gamma}^{\dagger}\boldsymbol{\Gamma}^{\dagger *} \\ &= 16\sigma_n^2[\boldsymbol{\Gamma}^{*}\boldsymbol{\Gamma}]^{-1}\boldsymbol{\Gamma}^{*}\boldsymbol{\Gamma}[\boldsymbol{\Gamma}^{*}\boldsymbol{\Gamma}]^{-1}. \end{aligned} \tag{44}$$

We can decompose $\boldsymbol{\Gamma}$ to

$$\boldsymbol{\Gamma} = \boldsymbol{\Xi}\boldsymbol{H} \tag{45}$$

and simplifying Eq. 44, we get

$$\tilde{\boldsymbol{R}}_n = \frac{16}{Q}\sigma_n^2(\boldsymbol{H}^*\boldsymbol{H})^{-1}. \tag{46}$$

Similar to the orthogonality based algorithm, the modified noise covariance matrix maintains its diagonal structure.

Both the proposed algorithms transform the sensor data to a modal domain. This transformation preserves the uncorrelated nature of the noise between different sensors with a similar uncorrelated behavior between the different modes. However, the noise is scaled by a factor which differs between the different modes. This noise scaling is symmetrical about the zeroth order, meaning that mode n and $-n$ undergo the same level of noise scaling. The higher the modulus of the order of a mode $|n|$ the lower the noise scaling.[4] Form the modifications that occur to the noise covariance matrix, we can conclude that both algorithms perform the same transformation on the sensor data.

5.2 Resolution

The angular resolution of DOA estimation methods depends on the number of sensors and the SNR. These DOA estimation methods relied on correlation of the phase vector of the source signal and the assumed phase if the signal was present at a test direction. If the test direction and the source direction were equal, a maximum value in the spectrum was obtained. In a similar manner, the two proposed algorithms localize sound sources based on the correlation of the received signal to the vector $\boldsymbol{c}(y, \phi)$. This subsection aims to present a theoretical analysis to the factors affecting resolution in the two proposed algorithms.

We start our analysis by assuming that the source signals are zero mean, Gaussian with variance, σ_s^2. The data covariance matrix in the eigen basis domain is

$$\boldsymbol{R} = \sigma_s^2\boldsymbol{c}(y, \Phi)\boldsymbol{c}^*(y_0, \phi_0) + \frac{16}{Q}\sigma_n^2(\boldsymbol{H}^*\boldsymbol{H})^{-1}. \tag{47}$$

To simplify the analysis, we assume there is only one source located at (y_0, ϕ_0). Using the identity for simplifying the inverse of a sum of matrices defined in [28, p. 490], the inverse of the covariance matrix is

$$\begin{aligned}\boldsymbol{R}^{-1} &= \frac{1}{a\sigma_n^2}(\boldsymbol{H}^*\boldsymbol{H})^{-1} \\ &\quad\times\left(\boldsymbol{I} - \frac{\boldsymbol{c}(y_0, \phi_0)\boldsymbol{c}^*(y_0, \phi_0)1/\left(a\sigma_n^2\right)(\boldsymbol{H}^*\boldsymbol{H})^{-1}}{\sigma_s^{-2} + \boldsymbol{c}^*(y_0, \phi_0)1/\left(a\sigma_n^2\right)(\boldsymbol{H}^*\boldsymbol{H})^{-1}\boldsymbol{c}(y_0, \phi_0)}\right)\end{aligned} \tag{48}$$

where $a = 16/Q$. Using Eqs. 48 and 24, the output from the MV spectrum can be derived as

$$\begin{aligned}Z^{-1}(y, \phi) &= \frac{1}{a\sigma_n^2}\Bigg(\boldsymbol{c}^*(y, \phi)\boldsymbol{H}^*\boldsymbol{H}\boldsymbol{c}(y, \phi) \\ &\quad - \frac{|\boldsymbol{c}^*(y, \phi)\boldsymbol{H}^*\boldsymbol{H}\boldsymbol{c}(y_0, \phi_0)|^2}{a\sigma_n^2/\sigma_s^2 + \boldsymbol{c}^*(y_0, \phi_0)\boldsymbol{H}^*\boldsymbol{H}\boldsymbol{c}(y_0, \Phi_0)}\Bigg).\end{aligned} \tag{49}$$

We define the inner product between two vectors, $\boldsymbol{a}$ and $\boldsymbol{b}$ as a scalar equivalent to $\boldsymbol{a}^*\boldsymbol{b}$ and is denoted by $\langle \boldsymbol{a}, \boldsymbol{b}\rangle$. The output of the MV spectrum Eq. 49 can be written in terms of the inner products of vectors as

$$\begin{aligned}Z^{-1}(y, \phi) &= \frac{1}{a\sigma_n^2}\Bigg(\langle \boldsymbol{H}\boldsymbol{c}(y, \phi), \boldsymbol{H}\boldsymbol{c}(y, \phi)\rangle \\ &\quad - \frac{|\langle \boldsymbol{H}\boldsymbol{c}(y, \phi), \boldsymbol{H}\boldsymbol{c}(y_0, \phi_0)\rangle|^2}{a\sigma_n^2/\sigma_s^2 + \langle \boldsymbol{H}\boldsymbol{c}(y_0, \phi_0), \boldsymbol{H}\boldsymbol{c}(y_0, \phi_0)\rangle}\Bigg).\end{aligned} \tag{50}$$

The modulus is introduced in Eq. 50 since $Z(y, \phi)$ is a real number. The maximum value of $Z(y, \phi)$ occurs at $y = y_0$ and $\phi = \phi_0$. It is important to mention that the MV spectrum obtained is the same whether we remove $\boldsymbol{H}$ or not. However, removal of $\boldsymbol{H}$ upper bounds the number of modes, M that we can use for a specified region of interest.

The MV spectrum has a peak at the source location which decreases gradually to a minimum, hence the 3dB point can be used to measure the sharpness of this decrease and give a good measure of the resolution of the proposed algorithms. The 3dB point occurs at (y, ϕ) satisfying

$$\frac{Z^{-1}(y_0, \phi_0)}{Z^{-1}(y, \phi)} = \frac{1}{2}. \tag{51}$$

For a large SNR, the 3 dB point is close to the source location, therefore

$$\langle \boldsymbol{H}\boldsymbol{c}(y, \phi), \boldsymbol{H}\boldsymbol{c}(y, \phi)\rangle \approx \langle \boldsymbol{H}\boldsymbol{c}(y_0, \phi_0), \boldsymbol{H}\boldsymbol{c}(y_0, \phi_0)\rangle = |b|^2. \tag{52}$$

[4]In this paper, the subscript n can refer to either noise or the mode, whenever ambiguity arises in the equations clarifications are provided in the description of these equations.

The peak of the MV spectrum occurs at $y = y_0$ and $\phi = \phi_0$, and using Eq. 52, we have

$$Z^{-1}(y_0, \phi_0) = \frac{1}{a\sigma_n^2}\left(|b|^2 - \frac{|b|^4}{a\sigma_n^2/\sigma_s^2 + |b|^2}\right)$$
$$= \frac{1}{a^2\sigma_n^4/\sigma_s^2 + a\sigma_n^2|b|^2}\left(\frac{a\sigma_n^2}{\sigma_s^2}|b^2|\right) \tag{53}$$

and

$$Z^{-1}(y, \phi) = \frac{1}{a^2\sigma_n^4/\sigma_s^2 + a\sigma_n^2|b|^2} \times \left(\frac{a\sigma_n^2}{\sigma_s^2}|b|^2 + |b|^4 - \left|\langle \boldsymbol{Hc}(y, \phi), \boldsymbol{Hc}(y, \phi)\rangle\right|^2\right). \tag{54}$$

Substituting Eqs. 53 and 54 into Eq. 51, we get

$$\frac{a\sigma_n^2/\left(\sigma_s^2\,|b|^2\right)}{a\sigma_n^2/\left(\sigma_s^2|b|^2\right)+1-\left|\langle \boldsymbol{Hc}(y,\phi),\,\boldsymbol{Hc}(y_0,\phi_0)\rangle\right|^2/|b|^4} = \frac{1}{2}. \tag{55}$$

The expression $\langle \boldsymbol{Hc}(y, \phi), \boldsymbol{Hc}(y_0, \phi_0)\rangle/|b|^2$ is the cosine of the angle between the vectors $\boldsymbol{Hc}(y, \phi)$ and $\boldsymbol{Hc}(y_0, \phi_0)$, we will denote this angle as ψ. In Eq. 55, the modulus value of the inner product bounds the values of $cos(\psi)$ between 1 and 0. When the angle between the two vectors is small, the inner product is close to 1 and when the inner product is close to 0 the angle is large. The angle between these two vectors at the 3dB increases as the SNR $\left(\sigma_s^2/\sigma_n^2\right)$ decreases and is more noticeable if we simplify Eq. 55 to

$$\left(\frac{|\langle \boldsymbol{Hc}(y, \phi), \boldsymbol{Hc}(y_0, \phi_0)\rangle|}{|b|^2}\right)^2 = 1 - \frac{16}{Q|b|^2}\frac{\sigma_n^2}{\sigma_s^2}. \tag{56}$$

The angle between $\boldsymbol{Hc}(y, \phi)$ and $\boldsymbol{Hc}(y_0, \phi_0)$ at the 3 dB point as a function of SNR is

$$\psi_{3dB} = cos^{-1}\left(\sqrt{1 - \frac{16}{Q|b|^2}\frac{\sigma_n^2}{\sigma_s^2}}\right) \tag{57}$$

and is valid only when $\sigma_s^2 > \sigma_n^2$. From Eq. 57, the resolution increases as ψ_{3dB} decreases, i.e., as the noise power decreases. In summary, the resolution is inversely proportional to ψ_{3dB}.

From the solution obtained the following remarks can be made

- The resolution is affected by the noise power which distorts the correlation point,
  $\boldsymbol{c}(y_0, \phi_0)$ in the sensor data and pushes this correlation point to overlap nearby correlation points $\boldsymbol{c}(y_0 + \delta, \phi_0 + \varsigma)$ where δ and ς are small in magnitude. Therefore the higher the noise power the lower the resolution and the larger the angle between the source location and the 3 dB vector.
- Increasing the sensors creates more noise averaging thus reducing the effective noise power. This results in a higher resolution and a similar effect can be observed in DOA algorithms.
- The radius at which the sensors are placed (radius of the chest) has an effect on the resolution, shown by the presence of $\boldsymbol{H}$ in Eq. 56. This factor of sensor radius is not present in DOA algorithms. From Fig. 5, we can observe that for two points within the sensor radius, the angle ψ decreases as the sensor radius is increased, hence the ψ_{3dB} occurs for points that are further apart. Therfore, the resolution decreases as sensor radius increases given that the radius of the region of interest is constant and thus the number of modes used remains the same.
- The matrices $\boldsymbol{H}$, $\boldsymbol{c}(y, \phi)$ and $\boldsymbol{c}(y_0, \phi_0)$ are dependent on the wavenumber, k and so dependent on the frequency. Testing for two points in close proximity, we can observe from Fig. 6 that as the frequency increases the angle between these two points (placed at different radii), ψ increases. A similar result was obtained for points at different angles. Therefore, an increase in frequency increases both the radial and the angular resolution of the proposed algorithms.

5.3 Nyquist Criteria

Consider Eq. 19 as a sampling scenario. Here coefficients of a signal with angular frequency n needs to be recovered given the sampling frequency is $2\pi/Q$. According to Nyquist's theorem, the sampling frequency

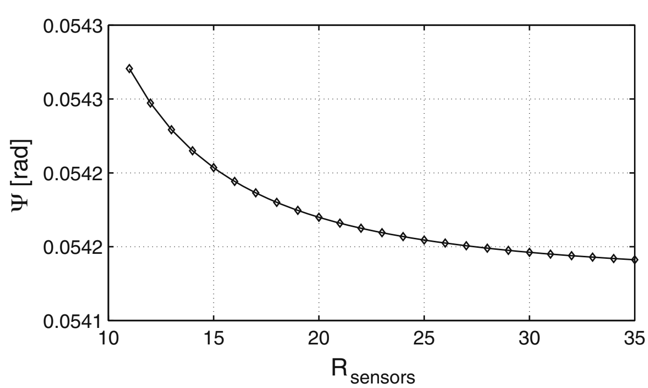

Figure 5 The decrease in angle, ψ, lower angular resolution as sensor radius increases, refer to Eqs. 56 and 57.

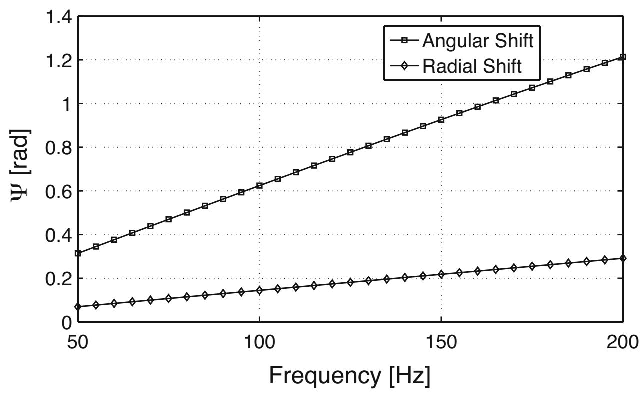

Figure 6 Increase in angle, ψ as frequency increases showing better angular and radial resolution when frequency is increased, refer to Eqs. 56 and 57.

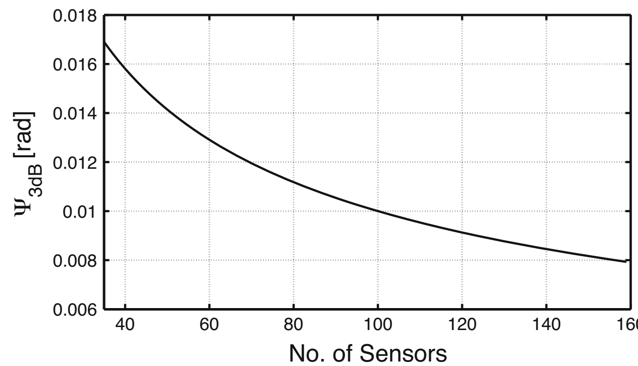

Figure 7 Variation of resolution with number of sensors for the source localizing algorithms.

must be greater than twice the highest frequency of the signal. Since we have Q sensors over 2π radians, we require

$$M < \frac{1}{2}Q. \tag{58}$$

Substituting Eq. 11 in Eq. 58 for an arbitrary radius, $\widetilde{R}$, Nyquist's criteria is satisfied if

$$\widetilde{R} < \frac{\lambda Q}{2\pi e}. \tag{59}$$

Works [29, 30] discussed spatial aliasing effects for the case of linear arrays. Spatial aliasing in linear arrays prevented localization of all sources. However, for localizing sources within a circular array, aliasing can be removed by reducing the radius of region, $\widetilde{R}$ where sources need to be located. As the frequency of sources increase, this radius reduces. This scenario contains an aliased region where $\widetilde{R} > \lambda Q/(2\pi e)$ and a non-aliased region where $\widetilde{R} < \lambda Q/(2\pi e)$.

The result from the Nyquist's criteria gives an important interpretation towards sensor position in localizing sources. Assuming that we want to localize all sources within a radius, $\widetilde{R}$ then from the Nyquist's criteria Eq. 59, the minimum number of sensors, $\widetilde{Q}$ required can be calculated. Further, these sensors can be placed at any radius greater that $\widetilde{R}$. Although, placing the sensors at a large radius can diminish their sensitivity to low power sources. In the sensor recordings noise is present, therefore increasing the number of sensors from $\widetilde{Q}$ results in a better resolution since the maximum likelihood estimations Eqs. 23 and 28 become more accurate.

5.4 Number of Sensors

If the number of sensors increases then the computation load goes up, however the effective noise covariance shown by Eqs. 43 and 46 is reduced which we term as noise averaging. The number of sensors must satisfy Nyquist's criterion Eq. 59 in order to localize sound source within a given radius. Further, the resolution of both the algorithm increases as the number of sensors increases, from Eq. 46 as $Q \to \infty$ then $\psi_{3dB} \to 0$ meaning the resolution is infinite. Provided that the Nyquist's criterion is satisfied fro $Q > 34$, the variation of ψ_{3dB} (resolution) as the sensor number increases for a SNR of 10 dB with source power set as unity is shown by Fig. 7. The improvement in resolution decreases as more and more sensors are added. Therefore, in designing a system the number of sensors to be used can be determined by a stopping criteria which states a minimum change in resolution.

6 Simulations

The simulations investigate the performance of the two proposed algorithms in localizing sound sources for different noise levels and for different frequencies. A circular array consisting of 40 uniformly spaced sensors on the circumference of a circle is used to record sounds from the sources. The radius of this circle is set to 8 units. The average chest diameter varies according to gender. The approximate average male and female chest diameters are 30 cm and 26 cm respectively [31]. To correspond to a male chest, 1 unit needs to represent 1.875 cm and for a female chest, 1 unit needs to represent 1.625 cm. We have used units since this allows the simulations to be scaled for a wide range of dimensions.

The source signals and the noise are modeled as stationary zero-mean white Gaussian processes. Further, the noise at each sensor is independent of the noise at any other sensor. The noise power received by the sensors is defined from the total signal power at the origin. For V sources, the SNR at each of the sensors is defined to be

$$SNR = 10\log_{10}\left[\frac{\sum_{v=1}^{V} P_{v,0}}{\sigma_N^2}\right] \tag{60}$$

where $P_{v,0}$ is the power of the v^{th} source at the origin and σ_N^2 is the noise power.

The simulations are performed with narrowband sources and for each trial 100 snapshots are taken. The recorded signals are then discrete Fourier transformed within the desired frequency band. Operations described in Section 4 are performed on the data set to obtain MV spectral estimates using the two proposed algorithms. The MV spectral estimate shows peaks at locations where sound sources are present. This paper will not investigate the effect of increasing the number of sensors or the number of snapshots. These factors were previously investigated in works [32, 33] for linear arrays.

The two proposed algorithms provide similar MV spectra and so for brevity, one set of results are illustrated in the following subsections.

6.1 Localizing Multiple Sources

The environment consists of eight uncorrelated sound sources placed at different radii. The marks "X"s in Fig. 8a. shows the actual locations of the eight sources. The SNR is set to 10 dB and the wavelength of the sources is 4 units. Scaling for an average male chest gives wavelength of the sound sources to be 7.5 cm. The speed of sound in lung parenchyma varies between 25–75 m/s [34]. Taking the lower speed, the frequency of the sound sources is 333 Hz. Gavriely et al reported spectral characteristics of normal lung sounds to lie approximately between 50 and 1000 Hz [35, 36]. For lung sound localization, the performance of the algorithms are considered for frequencies between 100 and 1000 Hz when velocity of the lung sounds can be considered isotropic. [15].

The use of units for the radius and wavelength can be considered to be a powerful representation and allows the spectrum obtained to be flexible. The dimensions of the chest varies from one person to another.

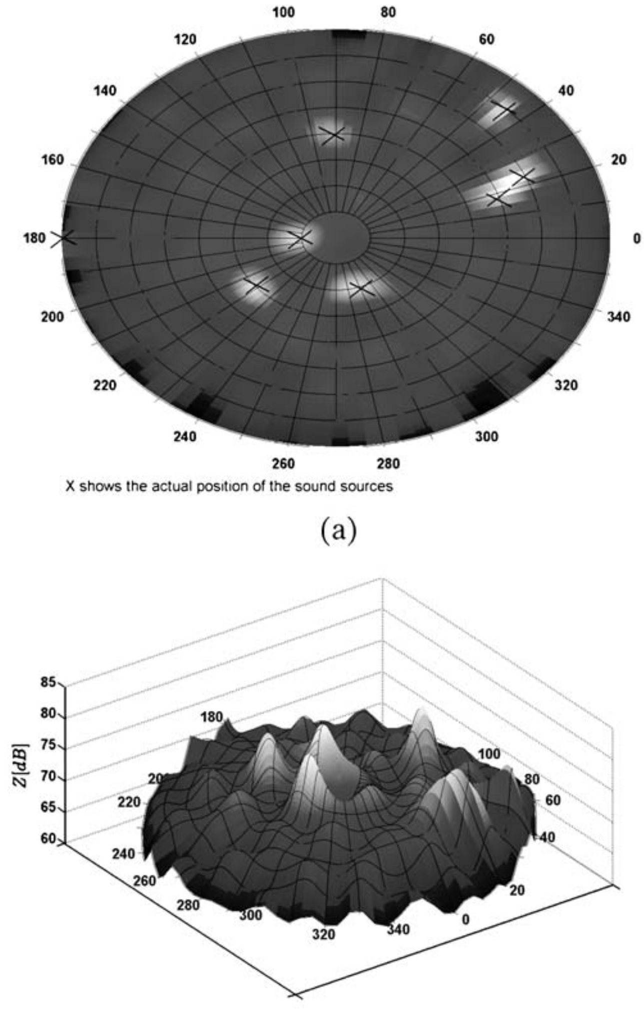

Figure 8 Spectrum for multiple 2-D sources with SNR = 10 dB. **a** X–Y view of the spectrum. This is a polar plot with angle versus radius. Successive concentric circles represent an increase of one unit of distance from the center. **b** 3-D plot of the spectrum.

Suppose a lung sound localization device providing a spectral estimate for different people represents the radius in units which can be scaled for application to the specific chest diameter (measured beforehand with a tape measure). Further, the speed of sound in the lung varies. Therefore, wavelength represented in units can be scaled and represented to frequencies for different speeds using the relationship $c = f\lambda$.

Peaks in the MV spectral estimate as illustrated in Fig. 8b. correspond accurately to actual source locations. In Fig. 8a, peaks are represented by the light colored regions. The peaks decrease in height as the radius is increased. Further, the source lying on equal radius as the sensors (radius = 8 units) cannot be detected by both proposed algorithms. Concerning resolution of the algorithms at 10 dB noise, the sources at radius of 5 and

6 are detected as one source since the resolution is not high enough to give two peaks.

6.2 Performance with Different Noise Levels and Number of Sensors

In the second scenario, the power of sound emitted by the eight sources is kept constant, but noise power is reduced by half to set the SNR to 20 dB. Even at a reduced noise power, the source at radius of 8 units cannot be detected.

Compared to the previous trial with SNR equal to 10 dB, the peaks corresponding to the source locations are higher and narrower. According to Eq. 57, this scenario has a resolution that is approximately two times larger than the previous scenario with SNR equal to 10 dB. This is illustrated by Fig. 9. where two distinct peaks are obtained for sources at radii of 5 and 6 units.

To check if the resolution increases with increasing the number of sensors, we left the noise power at 10 dB but increased the number of sensors to 80, the resulting spectrum is similar to that of decreasing the noise power to 20 dB. It is observed that the resolution is increased as compared to the spectrum in Fig. 8. This agrees with the theoretical result shown in Fig. 7.

6.3 Performance with Different Frequencies of Sound

In this scenario, the wavelength is increased to 7 units. Using dimensions of an average male chest and speed of sound in the chest as 25 m/s, this wavelength corresponds to a frequency of 190.5 Hz. Comparing Figs. 10 and 8, we can see that the resolution is reduced when the wavelength is increased or the frequency is reduced, agreeing with results obtained for the theoretical resolution analysis. Given that by experimental verification under a known wavelength and noise power the resolution can be determined, then Eq. 57 can use this initial resolution to give resolution of both algorithms for different wavelengths and noise power. Thus, the result obtained using Eq. 57 is important in the performance analysis of the proposed localizing algorithms.

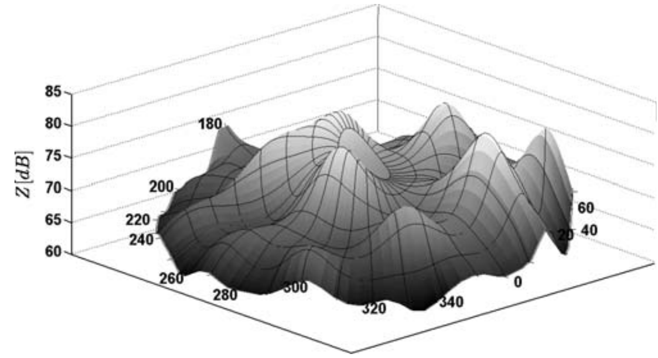

Figure 10 Spectrum showing a reduction in resolution when wavelength is increased.

In this trial, wavelength is reduced to 1 unit. As before, converting to an average male chest dimension, the frequency is increased to 1333 Hz. For lung sounds, this high a frequency does not have a high intensity. However, for the purpose of demonstrating aliasing for the proposed algorithms, we will use this frequency to show that simulation results obtained in Figs. 11 and 12 are in agreement with the Nyquist's criteria described in Subsection 5.3. The aliasing that occurs in localizing sources within a circular array is different from the aliasing that occurs for linear arrays. This difference in aliasing was discussed in Subsection 5.3. The simulation results illustrated by Figs. 11 and 12. prove that high frequencies causing aliasing with the region for which sources can be localized is reduced to $\widetilde{R}$. From simulation results $\widetilde{R}$ is approximately equal to 2.4 units and agrees to the result obtained by applying

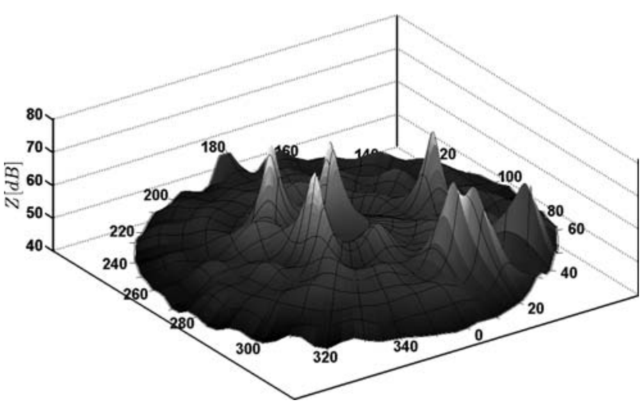

Figure 9 Spectrum obtained when SNR = 20 dB.

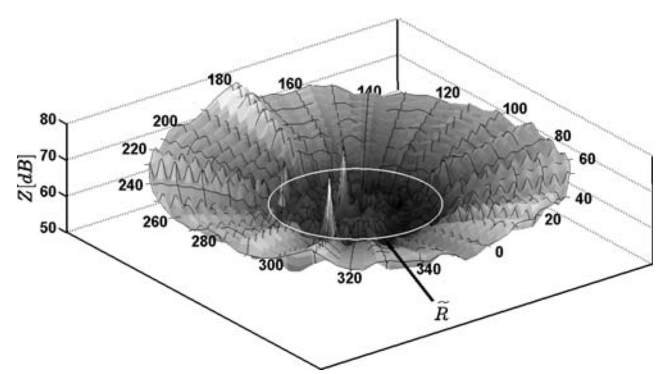

Figure 11 Spectrum showing aliasing when the wavelength is reduced. The region $\widetilde{R}$ for which sources can be localized is discernible.

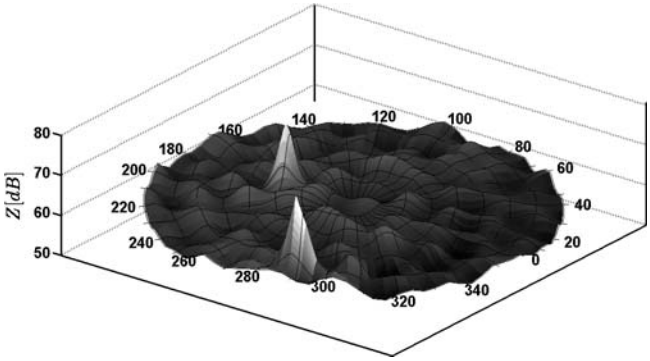

Figure 12 Spectrum of region $\widetilde{R}$ where two sound sources are present and each concentric circle represents a distance of 0.3 units.

Eq. 59 to this scenario. Further, within region $\widetilde{R}$, the resolution is higher than when the wavelength was equal to 4 units. In summary, simulations verify that increasing the frequency results in a higher resolution but reduces the radius of the region in which sources can be localized.

From simulation results presented in this subsection, several deductions to the performance of the algorithms can be made. These deductions are as follows:

- For a set up where the number of sensors and noise power is known, experimental determination of resolution at a certain frequency can be used to calculate the resolutions at other frequencies and noise powers using Eq. 57 for the proposed algorithms.
- For localizing sources within a frequency range, Eq. 59 can be applied to determine the radius of the region where sources can be located without aliasing.
- Given the radius of the region, minimum acceptable resolution and frequency range, the number of sensors can be determined using both Eqs. 57 and 59.

7 Comments and Comparison of the Proposed Algorithms

Lung sound measurements at multiple locations can give information on the lung sounds both spectrally, i.e. in the frequency domain and the regional distribution of the sounds. Alterations from the normal lung sounds can occur due lung injury or disease such as pneumothorax, lung consolidation, asthma and airway obstruction. These alterations involve a change in frequency content, quantifying and locating sounds for different frequency bins can be used to detect lung abnormalities [3, 37]. The two proposed algorithms can be modified to be used over the entire range of lung sounds by separating this frequency range into a set of narrowband frequency bins and then applying either one of the two proposed algorithms iteratively.

From the simulations presented in the previous section, it was shown that both the proposed algorithms have similar performance. The orthogonality based algorithm is less computationally expensive since it requires calculation of one matrix inverse whereas the least squares based algorithm involves calculating the inverse of two different matrices. Both algorithms perform the same transformation to the sensor data and the MV spectrum remains the same whether the contributions due the sensor radius is removed or not removed. However, not removing the sensor radius component increases the computational expense of the MV spectrum.

Further, the following comments pertaining to both proposed localizing algorithms can be made

- Both the localizing algorithms can work without previous estimates of source locations.
- Since both the algorithms calculate covariance matrices for the modified sensor recordings, other spatial spectral methods such as MUSIC or its variants can be applied instead of MV spectrum.
- For large sensor arrays and considering the frequency of sound, the dimension can be reduced to $2M + 1$ by converting to the eigen basis sets of a 2D wavefield. This reduces the computation expense of the proposed algorithms.

8 Conclusions

We have proposed two algorithms for localizing sound sources within a circular array of sensors by decomposing the wavefield to a set of eigen basis functions. These two algorithms can be applied for the purpose of acoustic imaging of the chest. However, in this paper we have assumed that the velocity of sound in the chest is isotropic. Future work will look at extending these algorithms for a layered cylindrical media that is characteristic of the chest and include reflections, refractions and standing waves.

The resolution of both algorithms increase with a decrease in noise power and increase with an increase in the frequency of the sound. We derived a theoretical relationship for resolution in terms of the noise level and frequency. Further, increase in frequency results in a reduction in the radius of the region for which sound sources are localized provided the number of sensors remain the same. This reduction in radius was a result of Nyquist's criteria applied to this scenario. The Nyquist's criteria and results from the resolution analysis can be applied in designing a localization system for the lung sounds given resolution, frequency range and noise power.

References

1. Ward, D. B., & Williamson, R. C. (1999). Beamforming for a source located in the interior of a sensor array. In *Proceedings of the fifth international symposium on signal processing and its applications, 1999. ISSPA '99* (Vol. 2, pp. 873–876). doi:10.1109/ISSPA.1999.815810.
2. Moussavi, Z. (2007). Acoustic mapping and imaging of thoracic sounds. In *Fundamentals of respiratory sounds and analysis* (Ch. 8, pp. 51–52). Morgan and Claypool.
3. Mansy, H. A., Hoxie, S. J., Warren, W. H., Balk, R. A., Sandler, R. H., & Hassaballa, H. A. (2004). Detection of pneumothorax by computerized breath sound analysis. *Chest, 126*(4), 881S.
4. Kompis, M., Pasterkamp, H., & Wodicka, G. R. (2001). Acoustic imaging of the human chest. *Chest, 120*(4), 1309–1321. doi:10.1378/chest.120.4.1309.
5. Charleston-Villalobos, S., Cortés-Rubiano, S., González-Camerena, R., Chi-Lem, G., & Aljama-Corrales, T. (2004). Respiratory acoustic thoracic imaging (rathi): Assessing deterministic interpolation techniques. *Medical & Biological Engineering & Computing, 42*(5), 618–626.
6. Charleston-Villalobos, S., Gonzalez-Camarena, R., Chi-Lem, G., & Aljama-Corrales, T. (2007). Acoustic thoracic images for transmitted glottal sounds. In *Engineering in medicine and biology society, 2007. EMBS 2007. 29th annual international conference of the IEEE* (pp. 3481–3484). doi:10.1109/IEMBS.2007.4353080.
7. Harris, F. J. (1978). On the use of windows for harmonic analysis with the discrete fourier transform. *Proceedings of the IEEE, 66*(1), 51–83.
8. Murphy, Jr., R. L. H. (1996). *Method and apparatus for locating the origin of intrathoracic sounds*. U.S. patent, 729,272.
9. McKee, A. M., & Goubran, R. A. (2005). Sound localization in the human thorax. In *Instrumentation and measurement technology conference, 2005. IMTC 2005. Proceedings of the IEEE* (Vol. 1, pp. 117–122). doi:10.1109/IMTC.2005.1604082.
10. Ozer, M. B., Acikgoz, S., Royston, T. J., Mansy, H. A., & Sandler, R. (2007). Boundary element model for simulating sound propagation and source localization within the lungs. *Journal of the Acoustical Society of America, 122*(1), 657–661.
11. Barshinger, J. N., & Rose, J. L. (2004). Guided wave propagation in an elastic hollow cylinder coated with a viscoelastic material. *IEEE Transactions on Ultrasonics, Ferroelectrics and Frequency Control, 51*(11), 1547–1556. doi:10.1109/TUFFC.2004.1367496.
12. Valle, C., Qu, J., & Jacobs, L. J. (1999). Guided circumferential waves in layered cylinders. *International Journal of Engineering Science, 37*(11), 1369–1387.
13. Yao, G.-J., Wang, K.-X., Ma, J., & White, J. E. (2005). Sh wavefields in cylindrical double-layered elastic media excited by a shear stress source applied to a borehole wall. *Journal of Geophysics and Engineering, 2*(2), 169–175. http://stacks.iop.org/1742-2140/2/169.
14. Abhayapala, T. D. (2006). Broadband source localization by modal space processing. In S. Chandran (Ed.), *Advances in direction-of-arrival estimation* (Ch. 4, pp. 71–86). Norwood: Artech House.
15. Wodicka, G., Stevens, K., Golub, H., Cravalho, E., & Shannon, D. (1989). A model of acoustic transmission in the respiratory system. *IEEE Transactions on Biomedical Engineering, 36*(9), 925–934.
16. Garbacz, R., & Pozar, D. (1982). Antenna shape synthesis using characteristic modes. *IEEE Transactions on Antennas and Propagation [legacy, pre-1988], 30*(3), 340–350.
17. Harackiewicz, F., & Pozar, D. (1986). Optimum shape synthesis of maximum gain omnidirectional antennas. *IEEE Transactions on Antennas and Propagation [legacy, pre-1988], 34*(2), 254–258.
18. Abhayapala, T. D., Kennedy, R. A., & Williamson, R. C. (2000). Nearfield broadband array design using a radially invariant modal expansion. *Journal of the Acoustical Society of America, 107*, 392–403.
19. Ward, D. B., & Abhayapala, T. D. (2004). Range and bearing estimation of wideband sources using an orthogonal beamspace processing structure. In *Proc. IEEE int. conf. acoust., speech, signal processing, ICASSP 2004* (Vol. 2(2), pp. 109–112).
20. Abhayapala, T. D., & Ward, D. B. (2002). Theory and design of high order sound field microphones using spherical microphone array. In *IEEE international conference on acoustics, speech, and signal processing, 2002. Proceedings. (ICASSP '02)* (Vol. 2, pp. 1949–1952).
21. Ward, D. B., & Abhayapala, T. D. (2001). Reproduction of a plane-wave sound field using an array of loudspeakers. *IEEE Transactions on Speech and Audio Processing, 9*(6), 697–707. doi:10.1109/89.943347.
22. Colton, D., & Kress, R. (1998). *Inverse acoustic and electromagnetic scattering theory* (2nd ed.). New York: Springer.
23. Jones, H. M., Kennedy, R. A., & Abhayapala, T. D. (2002). On dimensionality of multipath fields: Spatial extent and richness. In *IEEE international conference on acoustics, speech, and signal processing, 2002. Proceedings. (ICASSP '02)* (Vol. 3, pp. 2837–2840). doi:10.1109/ICASSP.2002.1005277.
24. Schmidt, R. (1986). Multiple emitter location and signal parameter estimation. *IEEE Transactions on Antennas and Propagation [legacy, pre-1988], 34*(3), 276–280.
25. Owsley, N. L. (1985). Sonar array processing. In S. Haykin (Ed.), *Array signal processing*. Englewood Cliffs: Prentice Hall.
26. Stewart, G. W. (1977). On the perturbation of pseudo-inverses, projections and linear least squares problems. *SIAM Review, 19*(4), 634–662. http://www.jstor.org/stable/2030248.
27. Li, F., & Vaccaro, R. J. (1992). Performance degradation of doa estimators due to unknown noise fields. *IEEE Transactions on Signal Processing, 40*(3), 686–690. doi:10.1109/78.120813.
28. Oppenheim, A. V. (1993). *Array signal processing: Concepts and techniques*. Englewood Cliffs: PTR Prentice Hall.
29. Dudgeon, D. E. (1977). Fundamentals of digital array processing. *Proceedings of the IEEE, 65*(6), 898–904.
30. Kummer, W. H. (1992). Basic array theory. *Proceedings of the IEEE, 80*(1), 127–140. doi:10.1109/5.119572.
31. Heinz, G., Peterson, L. J., Johnson, R. W., & Kerk, C. J. (2003). Exploring relationships in body dimensions. *Journal of Statistics Education, 11*(2).
32. Bresler, Y., & Macovski, A. (1986). On the number of signals resolvable by a uniform linear array. *IEEE Transactions on Acoustics, Speech, and Signal Processing,*

34(6), 1361–1375 (see also IEEE Transactions on Signal Processing).
33. Li, F., Liu, H., & Vaccaro, R. J. (1993). Performance analysis for doa estimation algorithms: Unification, simplification, and observations. *IEEE Transactions on Aerospace and Electronic Systems, 29*(4), 1170–1184. doi:10.1109/7.259520.
34. Rice, D. A. (1983). Sound speed in pulmonary parenchyma. *Journal of Applied Physiology, 54*(1), 304–308.
35. Gavriely, N., Palti, Y., & Alroy, G. (1981). Spectral characteristics of normal breath sounds. *Journal of Applied Physiology, 50*(2), 307–314.
36. Gavriely, N., Nissan, M., Rubin, A. H., & Cugell, D. W. (1995). Spectral characteristics of chest wall breath sounds in normal subjects. *Thorax, 50*(12), 1292–1300.
37. Royston, T. J., Zhang, X., Mansy, H. A., & Sandler, R. H. (2002). Modeling sound transmission through the pulmonary system and chest with application to diagnosis of a collapsed lung. *Journal of the Acoustical Society of America, 111*(4), 1931–1946.

S.M. Akramus Salehin completed his Bsc (Electrical and computer engineering) with first class honours from the University of Cape Town, South Africa in 2005 and was awarded the medal of merit by the Engineering Council of South Africa. He completed his masters by research from the same university in 2006 working on network layer protocols in the IP Multimedia Subsystems (IMS). In 2007, he completed his Masters by coursework in Information and Communication Technology at the Australian National University (ANU), Canberra. Currently, he is a PhD candidate at the Applied Signal Processing Group in the College of Engineering and Computer Science, ANU researching on nearfield source localization, beamforming, array signal processing and time-frequency analysis.

Thushara D. Abhayapala received the B.E. degree (with honors) in interdisciplinary systems engineering in 1994, and the Ph.D. degree in telecommunications engineering, both from the Australian National University (ANU), Canberra, in 1999. He was the Leader of the Wireless Signal Processing (WSP) Program at the National ICT Australia (NICTA) from November 2005 to June 2007. From 1995 to 1997, he was a Research Engineer with the Arthur C. Clarke Center for Modern Technologies, Sri Lanka. Since December 1999, he has been a faculty member with the Research School of Information Sciences and Engineering, ANU. Currently, he is an Associate Professor and the leader of the Applied Signal Processing Group.

His research interests are in the areas of audio and acoustic signal processing, space-time signal processing for wireless communication systems, and array signal processing. He has supervised 23 research students and co-authored approximately 150 peer-reviewed papers. He is currently an Associate Editor for the EURASIP Journal on Wireless Communications and Networking.